NJC

PAPER

View Article Online
View Journal | View Issue

Open Access Article. Published on 25 June 2025. Downloaded on 3/11/2026 6:26:33 AM.
This article is licensed under a Creative Commons Attribution-NonCommercial 3.0 Unported Licence.

Check for updates

Cite this: *New J. Chem.*, 2025, **49**, 12218

# A "turn-off" ICT-based optical probe for the selective detection of cyanide ions in real samples†

Sisay Uota,[a] Daniella Gross,[d] Bor-Jang Hwang,[c] Raymond Butcher,[b] Yousef Hijji,[ab] James Wachira,[c] Solomon Tadesse,[a] Jesse Edwards,[a] Kyle Edwards[d] and Fasil Abebe*[a]

Received 4th April 2025,
Accepted 18th June 2025

DOI: 10.1039/d5nj01489a

rsc.li/njc

A benzothiazolium-derived optical sensor, (*E*)-3-ethyl-2-(2,4,6-trimethoxystyryl) benzo[*d*]thiazol-3-ium iodide (**ETBI**), was synthesized for the selective detection of cyanide ions ($CN^-$). Its structure was confirmed through $^1$H NMR, $^{13}$C NMR, HRMS, IR, and single-crystal XRD analysis. **ETBI** exhibits a dual-mode optical response, displaying significant absorption, fluorescence quenching, and a distinct naked-eye-detectable color change from pale yellow to colorless. This change results from nucleophilic addition of $CN^-$ to the benzothiazolium ring, which disrupts the π-conjugated system and inhibits intramolecular charge transfer (ICT). The job plot indicated a 1:1 binding stoichiometry between **ETBI** and $CN^-$, with an association constant ($K_a$) of 2.86 × $10^4$ $M^{-1}$. The probe **ETBI** demonstrated high sensitivity, achieving a detection limit of 0.49 μM, well below the World Health Organization (WHO) guideline for $CN^-$ in drinking water. Furthermore, **ETBI** was successfully applied in fluorescence imaging of intracellular $CN^-$ in HeLa cells and using Whatman filter paper as a test strip.

## 1. Introduction

The development of simple, low-cost fluorogenic probes that are highly sensitive, selective, and optically active for detecting cyanide ions ($CN^-$) is very important for advancing bioenvironmental and chemical sciences.[1] $CN^-$ is extremely toxic to humans, even at low levels,[2] with lethal doses reported at as low as 0.5–3.5 mg per kilogram of body weight.[3] Consequently, the WHO has restricted the $CN^-$ concentration in drinking water to 1.9 μM.[4,5] Therefore, sensitive and reliable detection, quantification, and monitoring of $CN^-$ in biological and environmental matrices are critical.[1]

Various fluorogenic mechanisms have been utilized in the design of cyanide-selective probes,[6] including aggregation-induced emission (AIE),[7] fluorescence resonance energy transfer (FRET),[8] excited-state intramolecular proton transfer (ESIPT),[9,10] photoinduced electron transfer (PET),[11] and intramolecular charge transfer (ICT).[12–14] Among these, ICT-based sensors are particularly effective for $CN^-$ ion detection due to their simplicity, ease of synthesis, rapid response, and ability to provide efficient detection with minimal instrumentation, making them ideal for applications requiring quick and reliable results.[15] These sensors rely on the interaction between electron-donating and electron-withdrawing groups in small organic molecules, leading to significant changes in optical properties or color upon $CN^-$ binding that provide clear signals for $CN^-$ presence in the bioenvironmental system.[1]

Benzothiazolium-derivative fluorescent sensors are promising tools for $CN^-$ detection due to excellent optical properties, high sensitivity, and strong selectivity.[16] When integrated into ICT-based mechanisms, benzothiazolium derivatives enhance sensor performance by triggering a fluorescence change in response to $CN^-$ interactions, improving sensitivity and selectivity. In ICT systems, these sensors combine electron-donating and electron-withdrawing moieties covalently linked *via* a vinyl double bond. Nucleophilic addition to the benzothiazolium subunit interrupts the ICT process, leading to noticeable changes in spectral characteristics that induce measurable fluorescence changes through planar or twisted ICT mechanisms and color.[14,16]

The photophysical performance depends on molecular structure, allowing precise tuning of charge-transfer dynamics

[a] *Department of Chemistry, Morgan State University, 1700 E Cold Spring Ln, Baltimore, MD, 21251, USA. E-mail: fasil.abebe@morgan.edu*
[b] *Department of Chemistry, Howard University, 626 College Street NW, Washington, DC, 20059, USA*
[c] *Department of Biology, Morgan State University, 1700 E Cold Spring Ln, Baltimore, MD, 21251, USA*
[d] *Department of Chemistry, Towson University, 8000 York Road, Towson, MD 21252, USA*

† Electronic supplementary information (ESI) available. CCDC 2420824. For ESI and crystallographic data in CIF or other electronic format see DOI: https://doi.org/10.1039/d5nj01489a

 This journal is © The Royal Society of Chemistry and the Centre National de la Recherche Scientifique 2025

Open Access Article. Published on 25 June 2025. Downloaded on 3/11/2026 6:26:33 AM.
This article is licensed under a Creative Commons Attribution-NonCommercial 3.0 Unported Licence.

to amplify optical signals during $CN^-$ recognition. ICT-based benzothiazolium sensors are essential for selective and efficient $CN^-$ detection due to their structural simplicity and dual-wavelength fluorescence detection capabilities. These systems exhibit exceptional selectivity with minimal interference from competing anions, making them ideal for challenging environments like environmental monitoring and cellular bioimaging.[16–18]

In this context, we present the development of a new benzothiazolium-based $CN^-$ sensor, (*E*)-3-ethyl-2-(2,4,6-trimethoxystyryl) benzo[*d*]thiazol-3-ium iodide (**ETBI**). **ETBI** was designed and synthesized *via* a simple condensation reaction between 3-ethyl-2-methylbenzothiazolium iodide and 2,4,6-trimethoxybenzaldehyde. Its structure was fully confirmed through $^1$H NMR, $^{13}$C NMR, HRMS, IR, and single-crystal XRD spectral analysis, as well as the sensing mechanism, which was investigated using HRMS and IR titration, theoretical calculations, and Job's plot experiments. The sensor and optical properties of the **ETBI** molecule are explored through UV-Vis and fluorescence spectroscopy. Notably, this benzothiazolium-based probe, **ETBI**, has shown excellent performance in fluorescence imaging of $CN^-$ in HeLa cells and test strip-based detection, indicating its potential for real-time monitoring in biomedical and environmental applications.

## 2. Experimental

### 2.1. Materials and instruments

HeLa cells (CCL-2), originating from human epithelioid cervical carcinoma, were obtained from the American Type Culture Collection (ATCC; Manassas, Virginia, USA). All chemicals and analytical-grade solvents were purchased commercially and used as received, without further purification. Ultrapure water (approximately 18.2 MΩ-cm megaohm-centimeter) was used in all experiments. The stock solutions of anions of inorganic sodium salts ($CH_3COO^-$, $N_3^-$, $HSO_4^-$, $S^{2-}$, $S_2O_3^{2-}$, $ClO_3^-$, $NO_2^-$, $CO_3^{2-}$, $Br^-$, $F^-$, $Cl^-$, $I^-$, $OH^-$, $SCN^-$, $NO_3^-$, and $H_2PO_4^-$) and 3-ethyl-2-methylbenzothiazolium iodide were purchased from Sigma-Aldrich (Steinheim, Germany). Using a previously reported method, the synthesis was conducted in a microwave irradiation reactor (CEM Corporation, Matthews, NC).[18] The synthesized compound was monitored using thin-layer chromatography (TLC) on Silufol UV-254 plates with a 1 : 1 ethyl acetate–methanol mixture as the eluent. Spots were visualized under UV light. The melting point was measured using a standard digital apparatus (electrothermal, Fisher Scientific) without correction. $^1$H NMR and $^{13}$C NMR spectra were recorded on a Bruker Avance 400 MHz spectrometer, using tetramethylsilane (TMS) as the internal standard and DMSO-$d_6$ as the solvent. Liquid chromatography coupled with electrospray ionization-quadrupole-time of flight-high resolution mass spectrometry (LC-ESI-QTOF-HRMS) was used to obtain the mass spectra with an Agilent 6546 LC/Q-TOF spectrometer. Diode-array detection (DAD) and Q-TOF were UV and mass spectrometry detectors, respectively. Absorption and fluorescence spectra were collected using an Agilent Cary 60 UV/Vis spectrometer and a Cary Eclipse fluorescence spectrophotometer, respectively. The excitation and emission slit widths were set to 10 nm, and measurements were conducted in a 1 cm quartz cuvette with a 3 mL sample volume.

### 2.2. Stock preparation and analytical procedures

Dimethyl sulfoxide (DMSO) was selected to prepare the stock solutions of the sensor **ETBI**. For UV-Vis and fluorescence spectroscopy analyses, DMSO/$H_2O$ mixtures with ratios of 1 : 9 (v/v) and 1 : 1 (v/v), respectively, were used as the working solvents. The target anion ($CN^-$) and the potential competitive anions were prepared at $30 \times 10^{-2}$ M concentrations. The final working concentration for selectivity and competitive experiments was 10 μM **ETBI** and 1 mM anions. Fluorescence emission measurements were performed with 50 μM **ETBI** and 1 mM of $CN^-$ gradually added to complete the titration experiment. All spectroscopic analyses were conducted at room temperature. The experiments were performed in triplicate and repeated three times to ensure reproducibility.

### 2.3. Synthesis of (*E*)-3-ethyl-2-(2,4,6-trimethoxystyryl) benzo[*d*]thiazol-3-ium iodide (ETBI)

The sensor **ETBI** was synthesized based on a previously published method[18] using the condensation reaction between 3-ethyl-2-methylbenzothiazolium iodide (0.3052 g, 1 mmol) and 2,4,6-trimethoxybenzaldehyde (0.1962 g, 1 mmol), as shown in Scheme 1. Ethanol and piperidine were used as the reaction solvent and catalyst, respectively. The mixture was placed in a CEM Discovery microwave irradiation reactor,[19–21] under a pressure of 250 psi at 130 °C for 5 minutes. A red powdered product was obtained with a yield of 86%, m.p. 229 °C. $^1$H-NMR (400 MHz, DMSO-$d_6$), $\delta$ (ppm): 8.39 (m, 1H), 8.28 (m, 1H), 7.83 (m, 1H), 7.79 (d, 1H), 7.58 (d, 1H), 7.43 (s, 1H), 7.27 (s, 1H), 6.40 (s, 2H), 4.01 (s, 9H), 1.58 (t, 3H). $^{13}$C NMR (400 MHz, DMSO-$d_6$), $\delta$ (ppm): 173.24, 166.62, 164. 37, 162.74, 141.54, 140.11, 130.00, 128.32, 127.89, 124.65, 116.59, 111.02, 105.63, 92.13, 91.96, 57.17, 56.57, 56.38, 56.18, 13.93. HRMS (ESI): *m*/*z* calculated for $C_{20}H_{22}NO_3S^+$: 356.1315 $[M]^+$ and found: 356.1312.

### 2.4. DFT calculations method

Ground-state geometries of the molecules were optimized at the density functional theory (DFT) level using the hybrid B3LYP exchange–correlation functional with a DFT-optimized DZVP2 basis set.[22] Vibrational frequencies were calculated for the optimized structures to ensure the structures were at minima. TD-DFT[22,23] calculations were performed using the same functional and basis set to predict excited-state geometries and energies. All calculations were done in the gas phase

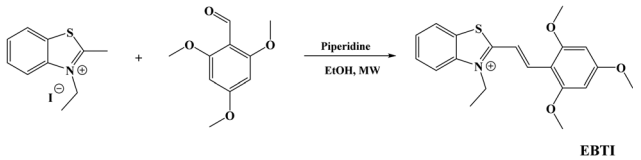


Scheme 1 Microwave-assisted synthesis of **ETBI**.

Open Access Article. Published on 25 June 2025. Downloaded on 3/11/2026 6:26:33 AM.
This article is licensed under a Creative Commons Attribution-NonCommercial 3.0 Unported Licence.

using a conductor-like screening model (COSMO) and water as the solvent.[24] All calculations were performed using the Gaussian 09 program package.[22] The calculations were performed on the HPC clusters at Towson University. Natural population analysis (NPA) was employed to generate natural atomic orbitals for the molecules of interest, which were calculated at the same level of theory as geometry optimization.

### 2.5. Cell culture and bioimaging

HeLa cell lines were used for cellular experiments. Following ATCC's protocol, the cells were cultured in Eagle's Minimum Essential Medium (EMEM, ATCC), supplemented with 10% fetal bovine serum[25] and 1% penicillin–streptomycin. Cultures were maintained at 37 °C in a humid atmosphere containing 5.0% $CO_2$. Fluorescence imaging was performed using a Leica STELLARIS 5 Confocal Microscope. Following the manufacturer's instructions, the MTS assay was conducted using the CellTiter 96® Aqueous One Solution Cell Proliferation Assay Kit (Promega, Madison, Wisconsin) for cytotoxicity evaluation. Briefly, 20 μL of MTS reagent was added to each well, and the cells were incubated at 37 °C in a humidified 5.0% $CO_2$ atmosphere for 2 hours.[26] Absorbance was then measured at 490 nm using a BioTek Synergy H1MF microplate reader.[21] All solutions and equipment were sterilized, and procedures were carried out under strictly aseptic conditions.

## 3. Results and discussion

### 3.1. Design and synthesis of ETBI

The sensor **ETBI** was synthesized by condensing 2,4,6-trimethoxybenzaldehyde and 3-ethyl-2-methylbenzothiazolium iodide in piperidine and ethanol. The microwave synthesis and sensor characterizations are described in the Experimental section and the ESI† (Fig. S3–S5). The structure of **ETBI** was confirmed by $^1$H NMR, $^{13}$C NMR, high-resolution mass spectrometry (HRMS), IR spectroscopy, and single-crystal X-ray diffraction techniques. The molecular structure of **ETBI** is composed of an electron-donating trimethoxy benzaldehyde group, attached to a benzothiazolium moiety, which acts as a solid electron-withdrawing moiety (Scheme 2). Cyanide's nucleophilic addition is expected at the carbon of the –C═N– bond in the benzothiazolium salt, breaking the π-conjugation and obstructing the ICT process.

### 3.2. Spectroscopic response of ETBI towards $CN^-$

Cyanide ions play a significant role in biological, environmental, and industrial processes,[27] making their sensitive and reliable detection essential. An effective sensor is preferable to perform well across a broad pH range to ensure wide applicability. To assess this, we studied the effect of pH on the absorbance of the **ETBI**–CN complex through the pH range of 4 to 12. It was found that the **ETBI** absorption behavior remained consistent over a wide pH range of 6 to 10, demonstrating that cyanide sensing performed well within this range, as shown in Fig. 2(a). The sensor ETBI was dissolved in a mixture of DMSO/HEPES in water at pH 7.0 for all experiments. The optical properties of compound **ETBI** were evaluated using UV-Vis and fluorescence spectroscopy. It showed an absorption peak at 435 nm and a fluorescence emission peak at 580 nm, respectively. The pH effect on the absorbance response of the **ETBI**–CN was investigated in the pH range of 4–12, where the **ETBI** absorption behavior remained similar over a wide pH range of 6–10, demonstrating that the sensing of cyanide performed well at this pH range, as shown in Fig. 2(a). The compound **ETBI** was dissolved in a mixture of DMSO/HEPES in water (1 : 9 v/v) at pH 7.0 for optical measurements. The absorption mainly originated from π–π* electron transfer and ICT process. The **ETBI** absorption studies were performed in the presence of competitive anions at room temperature. Only **ETBI** responded to $CN^-$ with a visible color change from pale yellow to colorless, while other anions such as $CH_3COO^-$, $N_3^-$, $HSO_4^-$, $S^{2-}$, $S_2O_3^{2-}$, $ClO_3^-$, $NO_2^-$, $CO_3^{2-}$, $Br^-$, $F^-$, $Cl^-$, $I^-$, $OH^-$, $SCN^-$, $NO_3^-$, and $H_2PO_4^-$ produced negligible interference, as illustrated in Fig. 1(a). Upon the incremental addition of $CN^-$, the peak intensity at 435 nm decreased significantly, while the peak near 270 nm showed an increase in intensity, as shown in Fig. 1(b). An isosbestic point at 300 nm indicated the formation of a new product between **ETBI** and $CN^-$. The nucleophilic attack of cyanide on the double bond in the benzothiazolium ring disrupted π-conjugation, thereby blocking intramolecular charge transfer and leading to a significant decrease in absorption, as illustrated in Fig. 1.

The fluorescence response of the sensor **ETBI** towards various anions was investigated in a 1 : 9 (v/v) DMSO/$H_2O$ mixture at pH 7.0. Fig. 2 shows the fluorescence spectra of **ETBI** with various anions, measured over a wavelength range of 400–700 nm at room temperature. Based on the results, a significant change in fluorescence intensity was observed for **ETBI**–CN at 580 nm, while other anions showed no significant change. This study, with the addition of $CN^-$ ions to the **ETBI** solution, demonstrated a change from a pale fluorescent (yellow) to a fluorescent blue color under UV light (inset: Fig. 2(a)). The selectivity and sensing capabilities of **ETBI** were verified through visual responses in both colorimetric and fluorescence methods. To gain insight into **ETBI**'s $CN^-$ sensing property, Fig. 2(b) displays a fluorescence titration of **ETBI** (10 μM) with $CN^-$, in which a gradual increase in $CN^-$ concentration, up to 10 equivalents, decreases fluorescence intensity. The observed changes in color and fluorescence during $CN^-$ detection indicate the efficiency of the **ETBI**, indicating its suitability for real-time applications.

**3.2.1. Time and concentration effect.** The effects of $CN^-$ concentration and reaction time on the sensing mechanism of **ETBI** were thoroughly investigated. A time-dependent

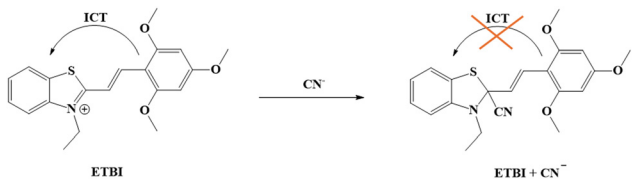


Scheme 2 Binding mechanism of **ETBI** with $CN^-$.

Open Access Article. Published on 25 June 2025. Downloaded on 3/11/2026 6:26:33 AM.
This article is licensed under a Creative Commons Attribution-NonCommercial 3.0 Unported Licence.

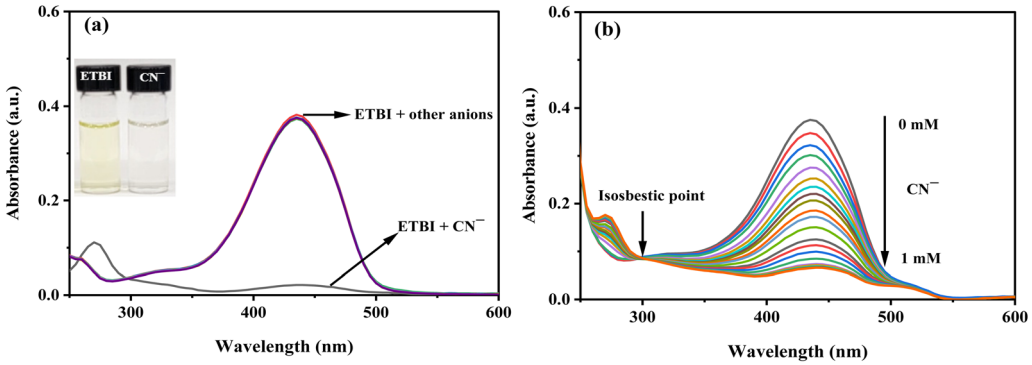


Fig. 1 (a) UV/Vis absorption spectra of **ETBI** (10 μM) in the presence of 10 equivalents of different anions in DMSO/$H_2O$ (1 : 9, v/v, 0.1 M HEPES; pH = 7.0). (b) titrated with $CN^-$ ion DMSO/$H_2O$ (1 : 9), v/v, 0.1 M HEPES; pH = 7.0.

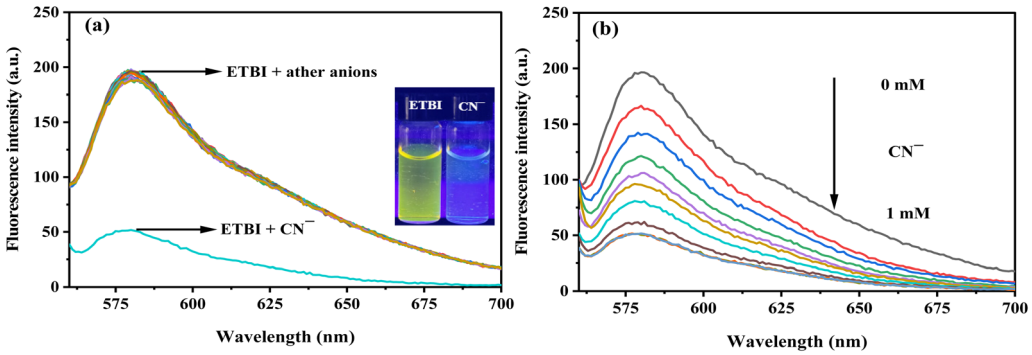


Fig. 2 Fluorescence spectra of **ETBI** (50 μM) (a) in the presence of 10 equivalents of anions (b) titrated with $CN^-$ ion DMSO/$H_2O$ (1 : 1), v/v, 0.1 M HEPES buffer, $\lambda_{ex}$ = 540 nm.

absorbance study was conducted using **ETBI** (10 μM) in the presence of $CN^-$ (1 mM) in a DMSO/$H_2O$ solution at room temperature. As shown in Fig. 3(b), the lowest absorbance intensity of **ETBI** was reached within 35 minutes. The three-dimensional (3D) response surface plot in Fig. 3(c) illustrates the dynamic relationship between absorbance, time, and $CN^-$ concentration. The absorbance of **ETBI** at 435 nm (*Z*-axis) was directly influenced by $CN^-$ concentration (*X*-axis) and reaction time (*Y*-axis). Increasing reaction time at $CN^-$ concentrations ranging from $1 \times 10^{-6}$ M to $1 \times 10^{-2}$ M resulted in a progressive absorbance decrease, accompanied by a visible color change from pale yellow to colorless.

At a concentration of $10^{-2}$ M, the reaction was completed within 8 minutes, demonstrating rapid interaction at higher cyanide concentrations. As the concentration was reduced to $10^{-3}$ M and $10^{-4}$ M, the reaction times were extended to 34 and 38 minutes, respectively, indicating a moderate reduction in the reaction rate. At lower concentrations of $10^{-5}$ M and $10^{-6}$ M, the reaction times were further prolonged to 68 minutes and 70 minutes, respectively, suggesting a significant deceleration of the reaction time. This trend highlights how lower CN concentrations are associated with reduced ICT efficiency and slower nucleophilic attack rates, thereby increasing the time required for reaction completion. Conversely, higher CN concentrations accelerate ICT blocking activity, as evidenced by the **ETBI**'s absorbance response, demonstrating a clear dependence on both time and concentration.

**3.2.2. Limit of detection (LOD) and limit of quantification (LOQ) analysis.** The LOD for $CN^-$ was determined using the formula $3.3\sigma/s$,[28] where $\sigma$ represents the standard deviation of the absorbance of the **ETBI** solution measured over 10 replicates (0.0006), and $s$ is the slope of the linear regression curve. A strong positive linear correlation between absorbance and $CN^-$ concentration was observed, with a coefficient of determination ($R^2$) of 0.993. The calculated LOD was 0.49 μM, significantly lower than the WHO permissible limit of 1.9 μM for $CN^-$ in drinking water. A comparison of **ETBI** with selected $CN^-$ sensing probes is provided in Table 1. The LOQ, calculated using the formula $10\sigma/s$,[18,28] was found to be 1.5 μM (Fig. 4(a)). Additionally, the association constant ($K_a$) was determined using a Benesi–Hildebrand plot, as described by eqn (1).

$$\frac{1}{(A - A_0)} = \frac{1}{K_a(A_{max} - A_0)[CN^-]} + \frac{1}{A_{max} - A_0}, \quad (1)$$

where $A/A_0$ is the absorbance at 435 nm of **ETBI** with/without $CN^-$, respectively, and $A_{max}$ is the absorbance of the **ETBI** solution at saturated concentration $CN^-$. $[CN^-]$ is the molar concentration of $CN^-$ to determine the $K_a$ of 2.86 × 104 $M^{-1}$,[29,30] utilizing the slope and *y*-intercept of the plot (Fig. 4(b)).

Open Access Article. Published on 25 June 2025. Downloaded on 3/11/2026 6:26:33 AM.
This article is licensed under a Creative Commons Attribution-NonCommercial 3.0 Unported Licence.

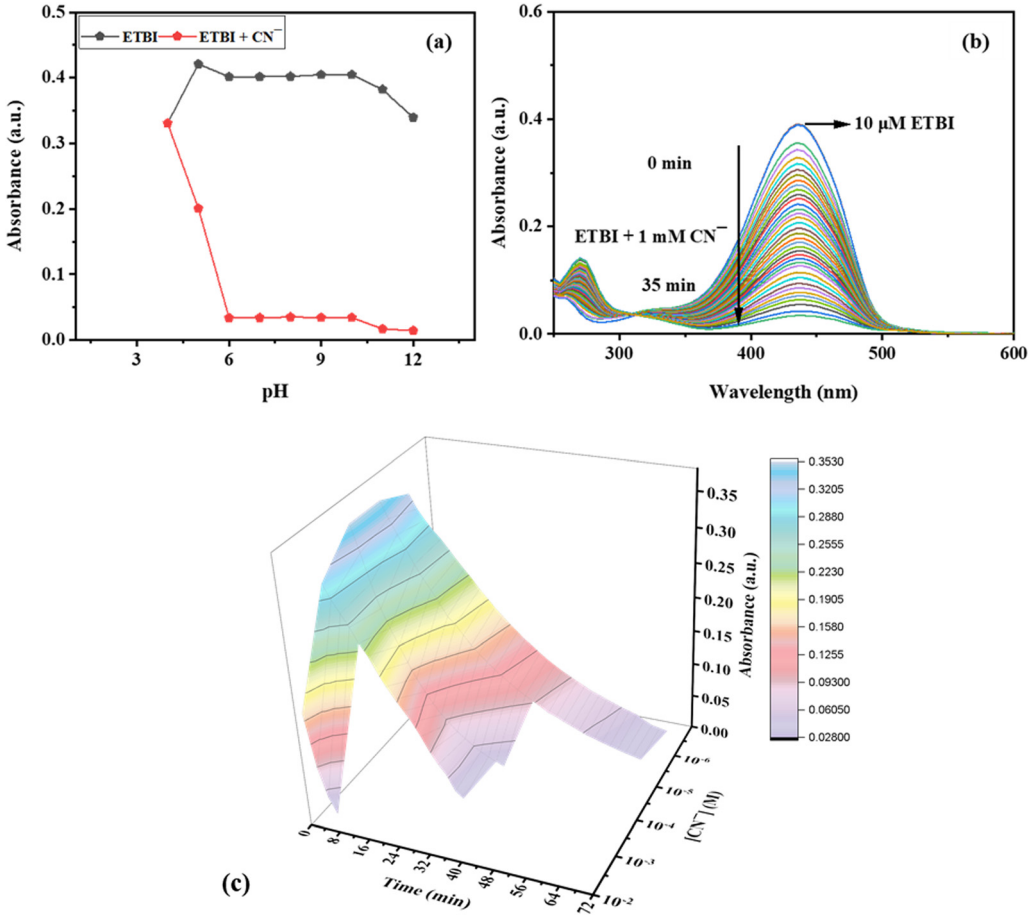


Fig. 3 (a) UV-Vis absorbance spectra of **ETBI** in the absence and presence of $CN^-$ as a pH function. (b) Time-dependent absorbance response of **ETBI** (10 μM) with 1 mM $CN^-$ in DMSO/$H_2O$ (1 : 9, v/v). (c) 3D response surface plot showing the effect of CN-concentration and reaction time on the absorbance of **ETBI** at 435 nm.

### 3.3. Selectivity and competitive experiments

To evaluate the selectivity of the sensor **ETBI** for $CN^-$ ions, competitive UV-Vis and fluorescence experiments were conducted in the presence of various other selected anions. Fig. 5 shows a competitive experiment conducted by adding $CN^-$ into the **ETBI** solution in the presence of 10 equivalent concentrations of various anions ($CH_3COO^-$, $N_3^-$, $HSO_4^-$, $S^{2-}$, $S_2O_3^{2-}$, $ClO_3^-$, $NO_2^-$, $CO_3^{2-}$, $Br^-$, $F^-$, $Cl^-$, $I^-$ $OH^-$, $SCN^-$, $NO_3^-$, and $H_2PO_4^-$). In the presence of competing analytes, the selectivity of $CN^-$ to **ETBI** was assessed using UV-Vis absorption at 435 nm and fluorescence intensity at 580 nm. The results show that interfering anions did not affect **ETBI**'s optical change in the presence of $CN^-$, indicating that the sensor **ETBI** maintained its selectivity towards $CN^-$. This behavior makes the **ETBI** sensor suitable for practical applications that detect cyanide ions, particularly in complex ionic environments.

### 3.4. Mechanistic insight into the $CN^-$ binding

The visible color and strong fluorescence of **ETBI** were attributed to its exceptional ICT effect, where the electron-donating 2,4,6-trimethoxybenzaldehyde group transfers electrons to the electron-accepting benzothiazolium moiety, as illustrated in Scheme 2. We analyzed a job plot using absorbance measurements to determine the binding mode between the sensor **ETBI** and $CN^-$. The highest absorbance at 435 nm was observed when the mole fraction of $CN^-$ was approximately 0.5, as shown in Fig. 6(a). The results suggest that $CN^-$ binds to **ETBI** in a 1 : 1 stoichiometry,[32,34] which is in good agreement with ESI-HRMS spectrometry analysis, as evidenced by mass signals at *m*/*z* [M] 356.1312 and [M + CN] *m*/*z* 383.3997 corresponding to **ETBI** and the **ETBI**–CN adduct, respectively, as shown in Fig. 7. The structure and binding mechanism were also further analyzed using FTIR spectroscopy of free **ETBI** and **ETBI**-CN. **ETBI** revealed clear and characteristic solid absorption bands for the –C═N– bond. This absorption peak completely disappeared for **ETBI**-CN, and a new, strong peak appeared at 2090 $cm^{-1}$, as shown in Fig. 6(b). These observations indicate the nucleophilic addition of the cyanide ion to the benzothiazolium group, as expected. This reaction process can sufficiently hinder the efficiency of the intramolecular charge transfer. Scheme 2 illustrates the ICT mechanism for the reaction between the sensor **ETBI** and the $CN^-$ ion, which is confirmed by the Job plot, ESI-HRMS, and FTIR.

### 3.5. Real-time detection of $CN^-$ using test strips

For real-time detection of $CN^-$, Whatman filter paper was used to prepare test strips by immersing it in a DMSO/$H_2O$ (1 : 9, v/v)

Open Access Article. Published on 25 June 2025. Downloaded on 3/11/2026 6:26:33 AM.
This article is licensed under a Creative Commons Attribution-NonCommercial 3.0 Unported Licence.

Table 1 Comparison of **ETBI** with selected $CN^-$ sensing probes

| Sensor's structure | Solvent system (v/v) | Detected anion | $\lambda_{max}$ (nm) | LOD (μM) | Ref. |
|---|---|---|---|---|---|
| 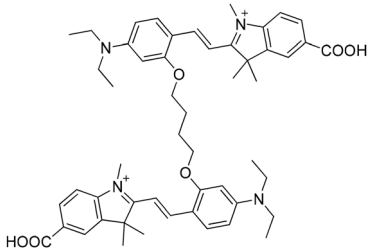 | $H_2O$ | $CN^-$ | 534 | 0.0153 | 31 |
| 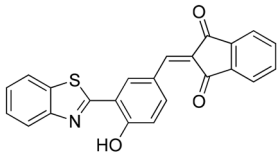 | $ACN/H_2O$ (7 : 3) | $CN^-$ | 398 | 0.00597 | 16 |
| 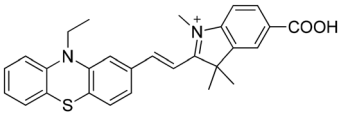 | $DMSO/H_2O$ (1 : 9) | | 563 | 6.47 | 32 |
| 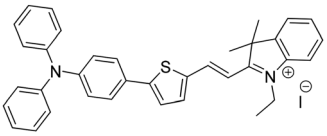 | $EtOH/H_2O$ (3 : 2) | $CN^-$ | 382 | 0.48 | 33 |
| 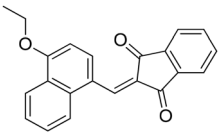 | $THF/H_2O$ (1 : 9) | $CN^-$ | 454 | 0.17 | 34 |
| 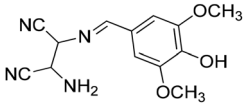 | $MeOH/H_2O$ (2 : 1) | $CN^-$ | 380 | 1.6 | 35 |
| 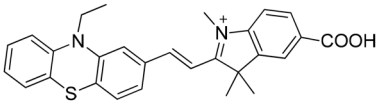 | $DMSO/H_2O$ (1 : 9) | $CN^-$ | 563 | 6.47 | 32 |
| 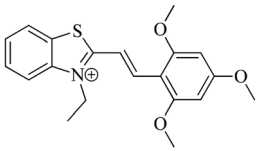 | $DMSO/H_2O$ (1 : 9) | $CN^-$ | 435 | 0.49 | This work |

solution of probe **ETBI** (50 μM), followed by air-drying.[36] When the test strip papers were exposed to various anions, a change from yellow to colorless was observed exclusively with $CN^-$, as shown in Fig. 8(a). For quantitative analysis, test strips were submerged in different $CN^-$ concentrations (0.2–1 mM), resulting in gradual color transition from yellow to colorless, as shown in Fig. 8(b). Therefore, the test strip approach, applying probe **ETBI**, offers a simple, rapid, selective, and cost-effective method for detecting $CN^-$ in environmental water samples without the need for expensive instrumentation.

### 3.6. Crystal structure of ETBI

At room temperature, slow evaporation of an **ETBI** solution in DMF–ethanol mixture resulted in the formation of shiny red crystals. The crystals were found to crystallize in the triclinic $P\bar{1}$ space group with crystallographic parameters including $a$ = 7.707 (10) Å, $b$ = 10.518 (10) Å, $c$ = 12.688 (10) Å, $\alpha$ = 97.407(10)°, $\beta$ = 91.858(10)°, and $\gamma$ = 93.375(10)° (Table 1). The single-crystal structure of **ETBI** (Fig. 9(a)) revealed that the benzothiazolium and 2,4,6-trimethoxybenzaldehyde moieties lie in the same plane. Several intermolecular interactions were observed in **ETBI**. The benzothiazolium S1 forms an S1···H bond interaction with a hydrogen bond length of 2.93 Å, resulting in a two-dimensional hydrogen bonding network (Fig. 9(b)). The units C2–H, C5–H, C7–H, C18–H, C19–H, and C20–H interact with the iodide (I1) unit, with bond lengths of 3.28, 3.18, 3.14, 3.22, 3.13, and 3.22 Å, respectively (Table S2, ESI†). The C10 and the methyl unit C18 form a C–H hydrogen bond interaction

Open Access Article. Published on 25 June 2025. Downloaded on 3/11/2026 6:26:33 AM.
This article is licensed under a Creative Commons Attribution-NonCommercial 3.0 Unported Licence.

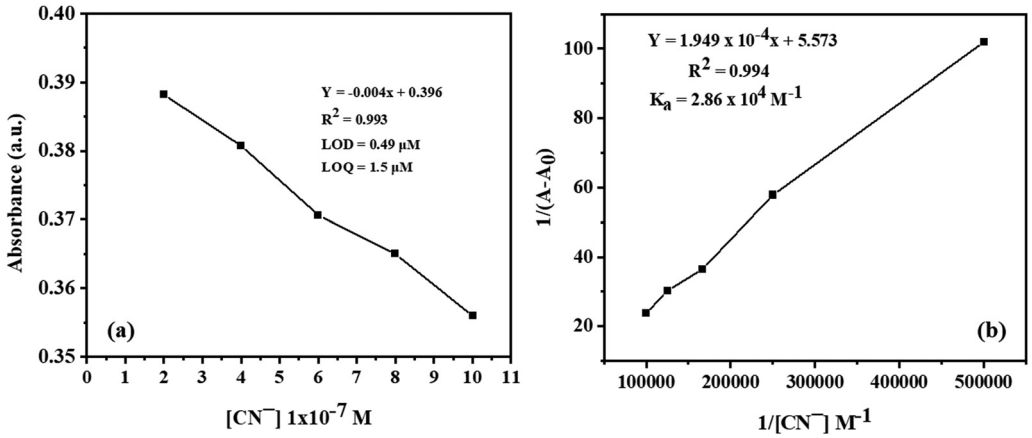


Fig. 4 (a) Determination of LOD and LOQ using UV/Vis spectroscopy at 435 nm. (b) Calculation of $K_a$ for the binding interaction between **ETBI** and $CN^-$ in DMSO/$H_2O$ (1 : 9, v/v).

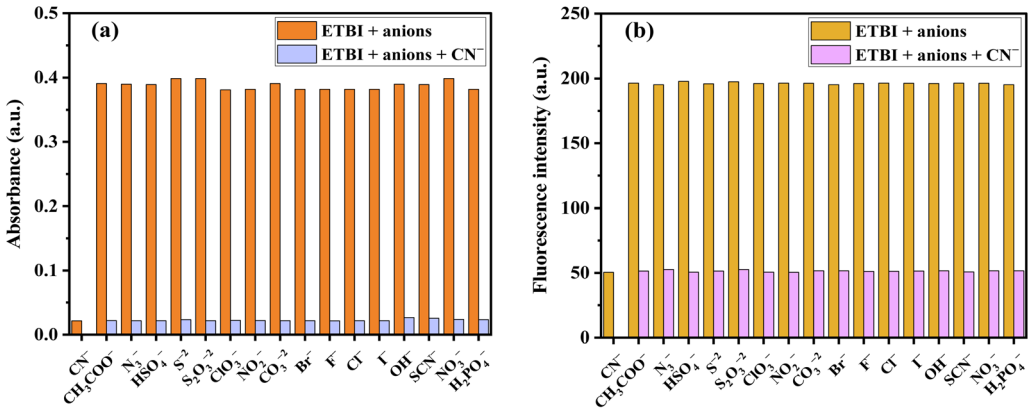


Fig. 5 (a) Change in the absorbance at 435 nm in DMSO/$H_2O$ (1 : 9, v/v) and (b) fluorescence intensities of **ETBI** at 580 nm ($\lambda_{ex}$ = 450 nm) upon addition of 10 equivalents of various anions in DMSO/$H_2O$ (1 : 1, v/v).

with O1 and O2, with bond lengths of 2.14 and 2.56 Å, respectively.

### 3.7. DFT calculation

Electronic structure calculations at the DFT level of theory were carried out on the **ETBI** molecule. Both the unbound cation and the CN-bound molecules were examined. These calculations were performed with a COSMO solvation model, with water selected as the solvent. Geometry optimizations were performed on both the ground and the first excited states. The optimized geometry is in excellent agreement with the crystal structure, with an N–C bond distance of 1.35 Å within the

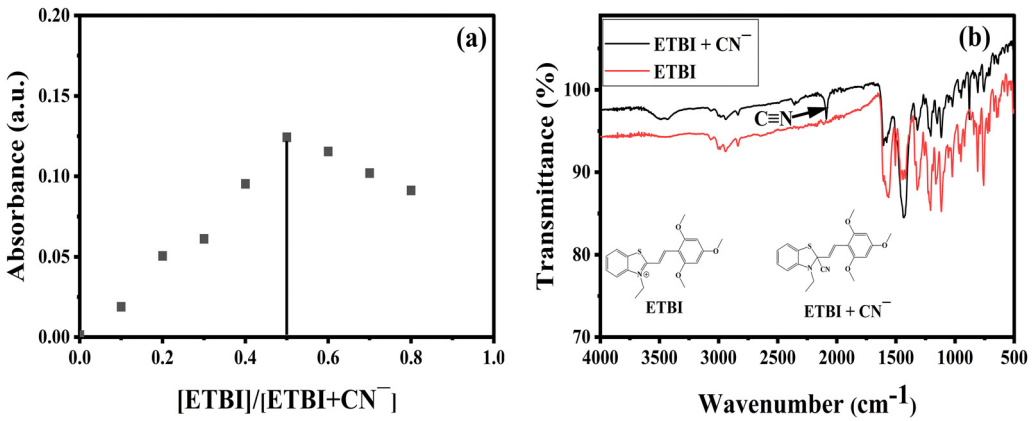


Fig. 6 (a) Job plot showing a 1 : 1 binding stoichiometry between **ETBI** and $CN^-$ ions. (b) FTIR spectra of free **ETBI** and in the presence of $CN^-$.

Open Access Article. Published on 25 June 2025. Downloaded on 3/11/2026 6:26:33 AM.
This article is licensed under a Creative Commons Attribution-NonCommercial 3.0 Unported Licence.

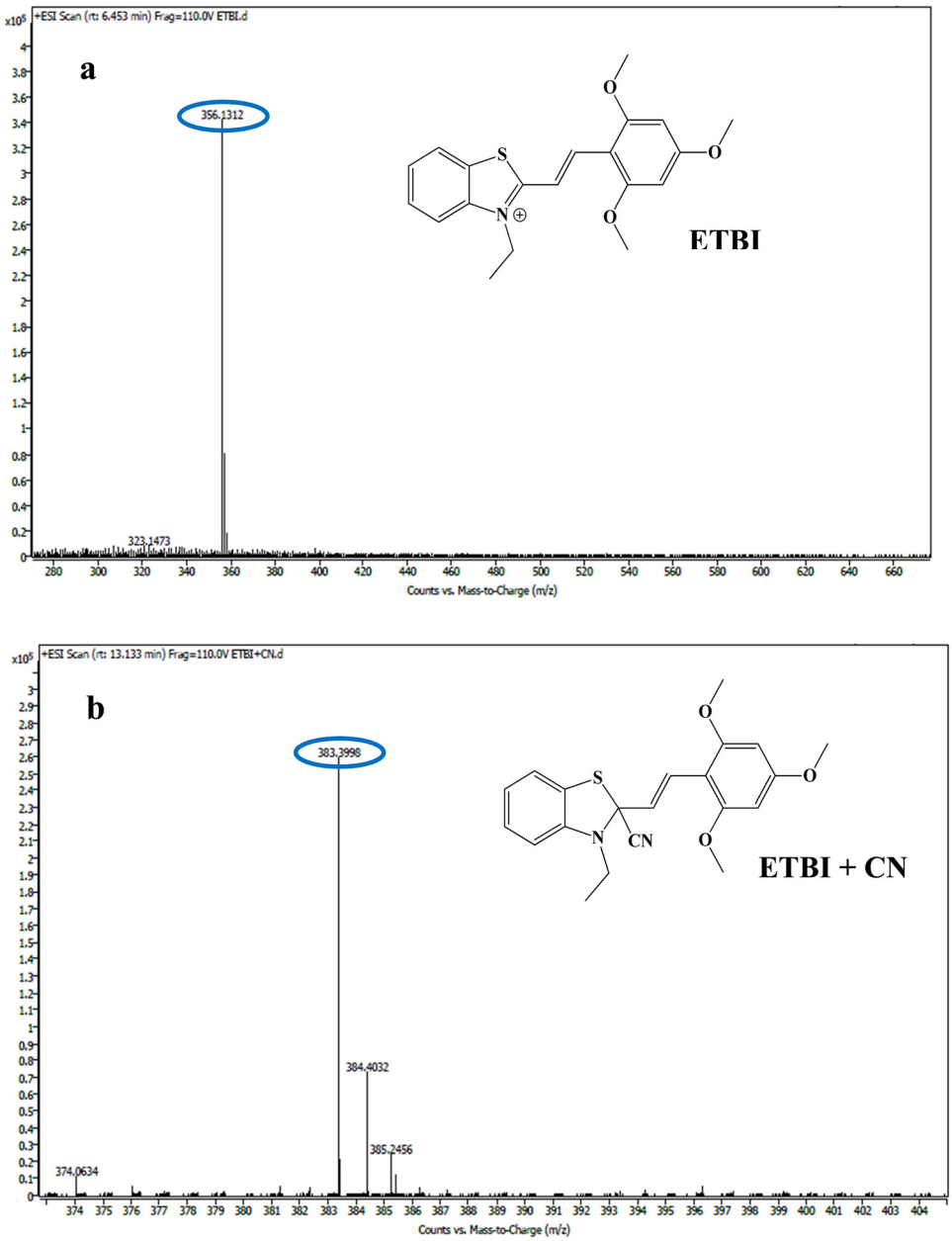


Fig. 7 HR-MS spectra of **ETBI** (a) and **ETBI**–CN adduct (b).

benzothiazolium ring (1.341 Å in the crystal structure). Upon binding $CN^-$, the calculated C–C bond length is 1.50 Å with a C–N bond length of 1.17 Å, typical of a cyanide group. The unbound **ETBI** molecule has a planar geometry distorted upon CN binding. A four-coordinate center is created, and the planar symmetry is broken as the methoxy functionalized ring is rotated perpendicular to the benzothiazolium ring, as shown in Fig. 10. This geometric distortion results in a significant change in the adsorption profile of the two molecules as well as a difference in the electron donation behavior between the methoxy-substituted ring and the benzothiazolium ring. The excited state structure of the **ETBI** molecule exhibits no significant differences from its ground state structure, except for a slight elongation (~0.02 Å) of the various bonds within the molecule.

A natural population analysis of the **ETBI** molecule was carried out, with both cyanide-bound and unbound structures. The difference in charge between individual atoms in the cyanide-bound molecule and the unbound molecule was examined, and the structures with partial charges assigned to the individual atoms are shown in Fig. 10. The binding of cyanide and subsequent rotation of the rings disrupts the conjugation between the aromatic rings. This limits the donation ability of the electron-rich methoxy-substituted ring; however, upon the nucleophilic attack of the $CN^-$, significantly more electron density is injected into the benzothiazolium system, which compensates for the loss in electronic donation from the methoxy-functionalized ring. The distinct electronic properties of the two structures lead to different singlet excitation behaviors, which are discussed in detail below.

Open Access Article. Published on 25 June 2025. Downloaded on 3/11/2026 6:26:33 AM.
This article is licensed under a Creative Commons Attribution-NonCommercial 3.0 Unported Licence.

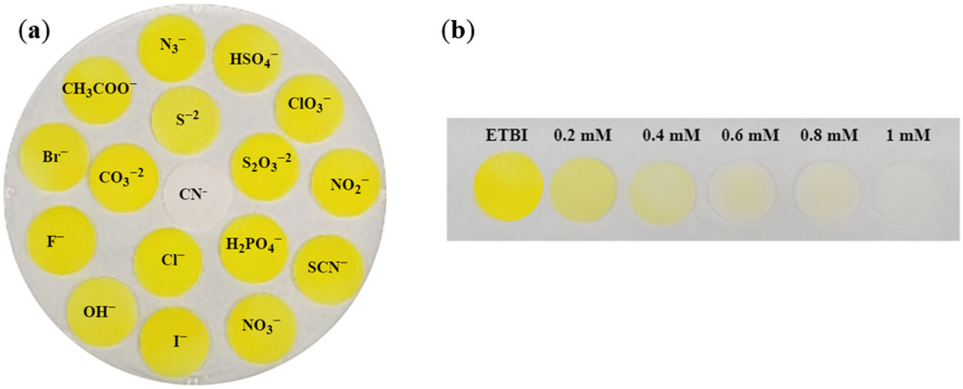


Fig. 8 (a) Color change of **ETBI** test strip upon immersing in $CN^-$ and various competing anion solutions. (b) Concentration-dependent color transition of the test strip from yellow to colorless with increasing $CN^-$ concentration.

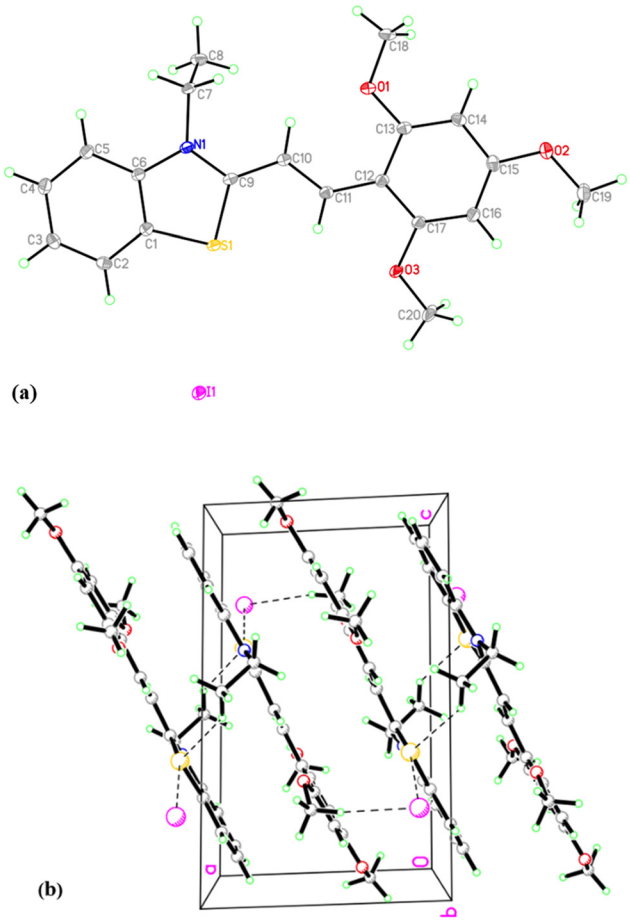


Fig. 9 Crystal structure of ligand **ETBI** (a) and intermolecular hydrogen bonding (b).

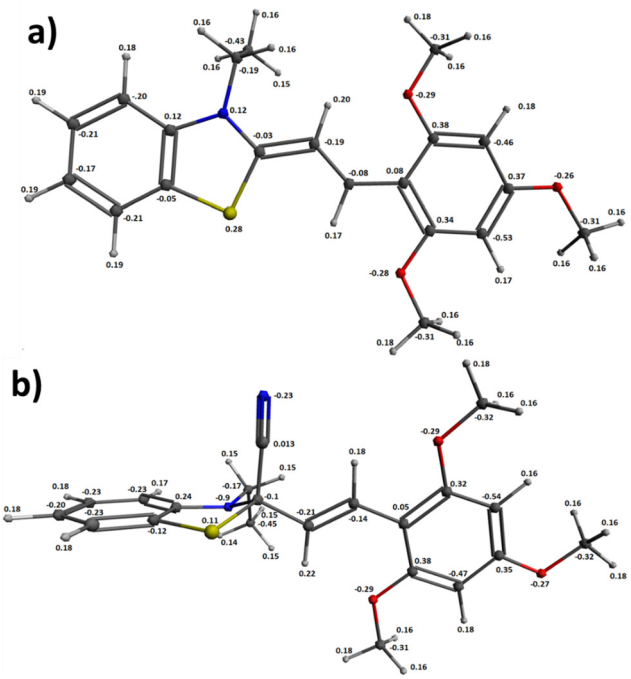


Fig. 10 Optimized structures of (a) **ETBI** and (b) **ETBI** with CN bound. Calculations were done at the B3LYP/DGDZVP2 level using the COSMO solvation model with water as the solvent. Partial charges assigned to individual atoms are shown adjacent to each atom.

Excited-state calculations were performed on the **ETBI** and **ETBI**–CN geometries. The first 20 singlet excitations were examined; the calculated energy differences, the corresponding wavelengths, and oscillator strengths are given in Tables S3 and S4 (ESI†). The excitation wavelength and oscillator strength were used to calculate UV absorption spectra for the molecules, as shown in Fig. S4 (ESI†). The first excitation in the unbound **ETBI** molecule corresponds to the HOMO–LUMO transition, resulting in intense absorption at ∼440 nm, which gives the molecule its characteristic yellow color. Upon binding of the $CN^-$, the 440 nm transition is lost, and the absorption profile changes. A moderately intense absorption in the ∼314 nm range corresponding to a mixture of the HOMO−1 to LUMO and the HOMO−1 to the LUMO+1 is responsible for the ∼310 nm absorption of the $CN^-$ bound structure resulting in its clear color upon binding $CN^-$. The excitations accountable for the visible absorptions in CN-bound and unbound molecules have high oscillator strength, resulting in high extinction

Open Access Article. Published on 25 June 2025. Downloaded on 3/11/2026 6:26:33 AM.
This article is licensed under a Creative Commons Attribution-NonCommercial 3.0 Unported Licence.

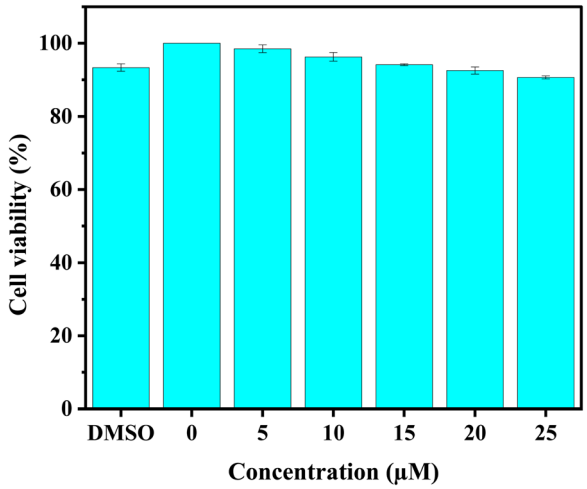


Fig. 11 Viability of HeLa cells in the presence of different concentrations of the **ETBI** probe. Cells were cultured with increasing concentrations of **ETBI** for 24 hours. The bars represent the means of independent quintuplicate experiments carried out three times. There were no significant differences in viability.

coefficients. This behavior is ideal for a candidate sensor to noticeably change color detectability without sophisticated equipment at potentially very low concentrations.

### 3.8. Cytotoxicity and cellular imaging

To assess the cytotoxic effects of **ETBI** on living cells, the MTS assay was conducted using HeLa cells seeded at a density of $2 \times 10^3$ cells per well in a 96-well plate. A 100 μL of cell culture medium containing the cells was added to each well and incubated overnight. The next day, cells were incubated with **ETBI** at concentrations of 0, 5, 10, 15, 20, and 25 μM for 24 h. The safety of DMSO at the highest concentration was also evaluated and confirmed to be non-toxic. Fig. 11 shows that concentrations up to 25 μM maintain over 90% cell viability, indicating that **ETBI** exhibits negligible cytotoxicity and supporting its potential application in biomedical fields.

Fluorescence imaging experiments were conducted on HeLa cell lines to further demonstrate the potential biological application of the **ETBI** probe as a sensor for $CN^-$ ions in living cells. Cells were seeded at a density of $2 \times 10^4$ cells per well in #1.5 polymer coverslip μ-Slide 4 Well chamber slides (Ibidi) and allowed to adhere overnight. Prior to staining, cells were washed twice with PBS and then incubated with 500 μL of 10 μM **ETBI** for 30 minutes at 37 °C. Fluorescence imaging of **ETBI**-treated cells was captured using a confocal laser scanning microscope. Then, the cells were treated with $CN^-$ for 30 minutes, and images were collected. As shown in Fig. 12, strong red fluorescence was detected in cells treated with **ETBI** alone, while fluorescence was quenched in the presence of $CN^-$ ions. A time-lapse imaging experiment was performed to investigate further the interaction of **ETBI** with 50 μM $CN^-$ in living cells using a stage-top incubator (Tokai-Hit), capturing images at 5-minute intervals. A progressive fluorescence quenching of **ETBI** was observed over 25 minutes in HeLa cells, as shown in Fig. 13. Quantification of fluorescence intensity was performed using the Fiji software package.[37,38] These findings confirm the potential of **ETBI** as a fluorescent probe for intracellular $CN^-$ detection and real-time bioimaging in living cells.

## 4. Conclusions

In conclusion, we designed and developed a benzothiazolium-conjugated optical probe, **ETBI**, exhibiting ICT properties, for the selective detection of cyanide ions. The sensor **ETBI** exhibits excellent selectivity for cyanide over other interfering anions, primarily due to cyanide's nucleophilic attack on the benzothiazolium ring's carbon. The structure of **ETBI** was confirmed using advanced analytical techniques, including $^1$H NMR, $^{13}$C NMR, HRMS, and single-crystal X-ray diffraction (XRD). The sensing mechanism was investigated through UV-Vis, fluorescence, ESI-

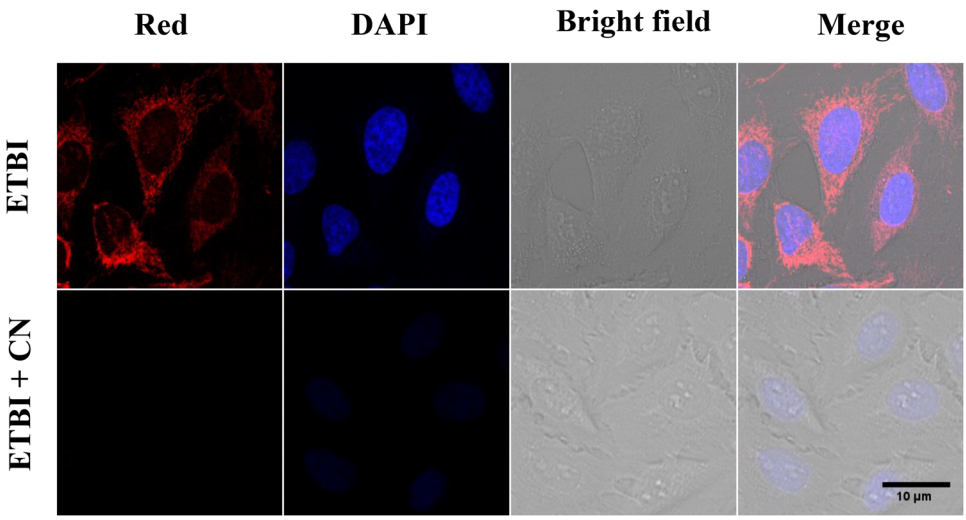


Fig. 12 Fluorescence imaging of HeLa cells cultured with the probe **ETBI** (10 μM), followed by treatment with $CN^-$ (50 μM). The cell nuclei were stained with 100 ng $mL^{-1}$ of DAPI.

Open Access Article. Published on 25 June 2025. Downloaded on 3/11/2026 6:26:33 AM.
This article is licensed under a Creative Commons Attribution-NonCommercial 3.0 Unported Licence.

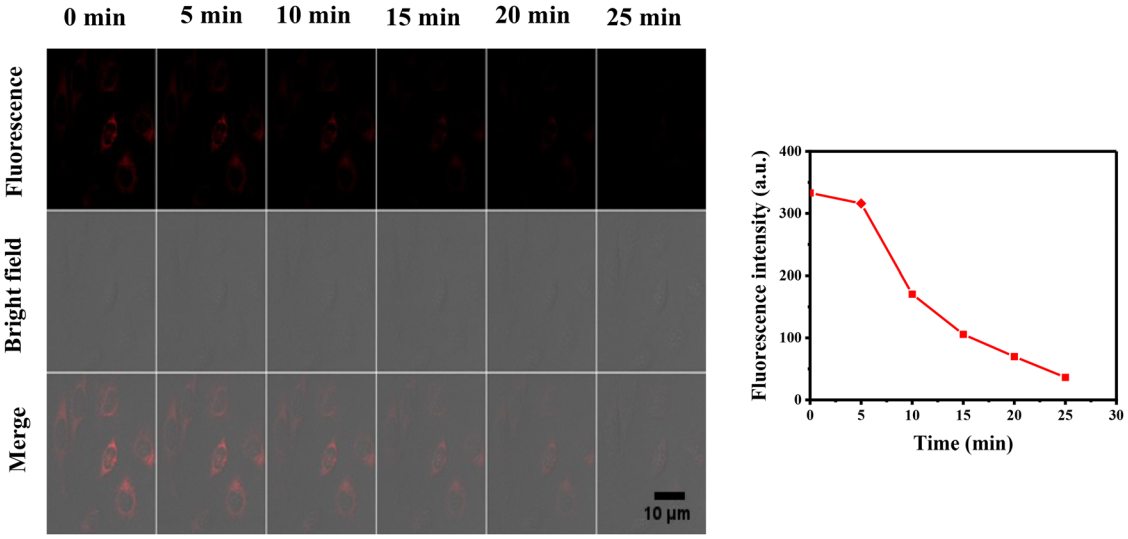


Fig. 13 Time-lapse fluorescence imaging of **ETBI** (10 μM) in live HeLa cells treated with $CN^-$ (50 μM) at 5-minute intervals, along with fluorescence intensity quantification.

MS, and FTIR titrations, revealing a 1 : 1 binding stoichiometry. The probe exhibited a detection limit well below the WHO guideline for cyanide in drinking water. Its practical real-time applicability was demonstrated through test strip assays and intracellular imaging of $CN^-$ in HeLa cells.

## Author contributions

Sisay Uota: conceptualization, methodology, investigation, software, data curation, writing – original draft. Daniella Gross: investigation, visualization. Bor-Jang Hwang: methodology. Raymond Butcher: methodology and investigation. Yousef Hijji: conceptualization, methodology, resources, co-supervision. James Wachira: methodology, resources, writing – review & editing. Solomon Tadesse: methodology, resources, Jesse Edwards: methodology, resources, Kyle Edwards: methodology, investigation, resources, writing – review & editing. Fasil Abebe: conceptualization, methodology, resources, data curation, funding acquisition, project administration, supervision, writing – original draft.

## Conflicts of interest

The authors declare that they have no known competing financial interests or personal relationships that could have appeared to influence the work reported in this paper.

## Data availability

The data supporting the findings of this study are available in the ESI† file accompanying this article.

## Acknowledgements

This research was funded by the National Science Foundation's Division of Chemistry under grant [2100629]. The authors acknowledge Morgan State University's Molecular and Cellular Biology core lab for providing instruments [5U54MD013376 and 5UL1GM118973].

## References

1 D. Lyngdoh Lyngkhoi and S. Khatua, A coumarin containing hemicyanine-based probe for dual channel detection of cyanide ion, *Inorg. Chim. Acta*, 2024, **572**, 122300, DOI: 10.1016/j.ica.2024.122300.
2 L. Xue, R. Wang, S. Qi, H. Xu, X. Wang, L. Wu, Q. Yang, J. Du and Y. Li, A novel 100% aqueous solution near-infrared ratiometric fluorescent CN-probe based on 1,4-dihydropyridines, with a large fluorescent emission peak shift, *Talanta*, 2021, **225**, 122100, DOI: 10.1016/j.talanta.2021.122100.
3 M. Saremi, A. Kakanejadifard, M. Ghasemian and M. Adeli, A colorimetric and turn-on fluorescent sensor for cyanide and acetate-based Schiff base compound of 2,2′-((1*E*,11*E*)-5,8-dioxa-2,11-diazadodeca-1,11-diene-1,12-diyl)bis(4-((*E*)-phenyldiazenyl)phenol), *Spectrochim. Acta, Part A*, 2023, **292**, 122397, DOI: 10.1016/j.saa.2023.122397.
4 F. A. M. Al-Zahrani, R. M. El-Shishtawy, A. M. Asiri, A. M. Al-Soliemy, K. A. Mellah, N. S. E. Ahmed and A. Jedidi, A new phenothiazine-based selective visual and fluorescent sensor for cyanide, *BMC Chem.*, 2020, **14**, 2, DOI: 10.1186/s13065-019-0656-x.
5 M. Acar, A. Daştan and R. Koçak, Fluorometric and colorimetric sensor for selective detection of cyanide anion by dibenzosuberenone-based dihydropyridazine in aqueous solution, *Talanta*, 2024, **277**, 126241, DOI: 10.1016/j.talanta.2024.126241.

 This journal is © The Royal Society of Chemistry and the Centre National de la Recherche Scientifique 2025

Open Access Article. Published on 25 June 2025. Downloaded on 3/11/2026 6:26:33 AM.
This article is licensed under a Creative Commons Attribution-NonCommercial 3.0 Unported Licence.

6 M. Ilakiyalakshmi, K. Dhanasekaran and A. A. Napoleon, A Review on Recent Development of Phenothiazine-Based Chromogenic and Fluorogenic Sensors for the Detection of Cations, Anions, and Neutral Analytes, *Top. Curr. Chem.*, 2024, **382**, 29, DOI: 10.1007/s41061-024-00474-9.

7 P. Wang, S. Cao, T. Yin and X.-L. Ni, Unprecedented tunable hydrophobic effect and anion recognition triggered by AIE with Hofmeister series in water, *Chin. Chem. Lett.*, 2021, **32**, 1679–1682, DOI: 10.1016/j.cclet.2020.11.068.

8 K. Prakash, P. Ranjan Sahoo and S. Kumar, A fast, highly selective and sensitive anion probe stemmed from anthracene-oxazine conjugation with $CN^-$ induced FRET, *Dyes Pigm.*, 2017, **143**, 393–400, DOI: 10.1016/j.dyepig.2017.04.060.

9 B. Kuzu, Z. Ekmekci, M. Tan and N. Menges, Excited State Intramolecular Proton Transfer (ESIPT)-Based Sensor for Ion Detection, *J. Fluoresc.*, 2021, **31**, 861–872, DOI: 10.1007/s10895-021-02716-1.

10 S. Paul and P. Banerjee, An ESIPT based turn on fluorochromogenic sensor for low level discrimination of chemically analogous $Zn^{2+}$ and $Cd^{2+}$ & aqueous phase recognition of bio-hazardous $CN^-$: From solution state analysis to prototype fabrication, *Sens. Actuators, B*, 2021, **329**, 129172, DOI: 10.1016/j.snb.2020.129172.

11 W.-J. Qu, W.-T. Li, H.-L. Zhang, T.-B. Wei, Q. Lin, H. Yao and Y.-M. Zhang, A rational designed fluorescent and colorimetric dual-channel sensor for cyanide anion based on the PET effect in aqueous medium, *Sens. Actuators, B*, 2017, **241**, 430–437, DOI: 10.1016/j.snb.2016.10.100.

12 P. R. Lakshmi, R. Manivannan, P. Jayasudha and K. P. Elango, An ICT-based chemodosimeter for selective dual channel sensing of cyanide in an aqueous solution, *Anal. Methods*, 2018, **10**, 2368–2375, DOI: 10.1039/C8AY00818C.

13 U. Reddy Gandra, R. Lo, P. Managutti, A. Mannan Butt, P. Sreekanth Reddy, A. Qurashi, S. Mohamed and M. I. H. Mohideen, ICT-Based Fluorescent Nanoparticles for Selective Cyanide Ion Detection and Quantification in Apple Seeds, *Analyst*, 2024, 489–497, DOI: 10.1039/D4AN01265H.

14 X.-M. Song, H.-F. Ye, J.-L. Song, Y.-J. Xi and Y. Wu, A novel "turn on" fluorescent and colorimetric ICT-based sensor for the detection of fluoride and cyanide ions, *J. Photochem. Photobiol., A*, 2025, **459**, 116069, DOI: 10.1016/j.jphotochem.2024.116069.

15 R. AbhijnaKrishna, S.-P. Wu and S. Velmathi, On-spot detection of diethylchlorophosphate through device fabrication, pen and spray method based on intramolecular charge transfer modulated sensor molecule extending application to cell imaging, *Microchem. J.*, 2024, **205**, 111369, DOI: 10.1016/j.microc.2024.111369.

16 D. Jothi, S. Munusamy, S. M. Kumar, S. Enbanathan and S. K. Iyer, A benzothiazole-based new fluorogenic chemosensor for the detection of CN − and its real-time application in environmental water samples and living cells, *RSC Adv.*, 2022, **12**, 8570–8577, DOI: 10.1039/D1RA08846G.

17 R. Caputo, M. L. Calabrò, N. Micale, A. D. Schimmer, M. Ali, M. Zappalà and S. Grasso, Synthesis of benzothiazole derivatives and their biological evaluation as anticancer agents, *Med. Chem. Res.*, 2012, **21**, 2644–2651, DOI: 10.1007/s00044-011-9789-8.

18 S. Uota, B.-J. Hwang, R. Butcher, R. Mullins, J. Wachira, Y. Hijji and F. Abebe, A simple benzothiazolium-based sensor for cyanide detection: Applications in environmental analysis and bioimaging, *Spectrochim. Acta, Part A*, 2024, 125155, DOI: 10.1016/j.saa.2024.125155.

19 O. Aduroja, R. Shaw, S. Uota, I. Abiye, J. Wachira and F. Abebe, A Novel Fluorescent Chemosensor Based on Rhodamine Schiff Base: Synthesis, Photophysical, Computational and Bioimaging Application in Live Cells, *Inorganics*, 2025, **13**, 5, DOI: 10.3390/inorganics13010005.

20 F. Abebe, P. Perkins, R. Shaw and S. Tadesse, A rhodamine-based fluorescent sensor for selective detection of $Cu^{2+}$ in aqueous media: Synthesis and spectroscopic properties, *J. Mol. Struct.*, 2020, **1205**, 127594, DOI: 10.1016/j.molstruc.2019.127594.

21 O. Aduroja, I. Abiye, A. Fathima, S. Tadesse, B. Ozturk, J. Wachira and F. Abebe, Microwave-assisted synthesis for a highly selective rhodamine 6G-derived fluorescent sensor and bioimaging, *Inorg. Chem. Commun.*, 2023, **147**, 110236, DOI: 10.1016/j.inoche.2022.110236.

22 F. Abebe, T. Sutton, P. Perkins and R. Shaw, Two colorimetric fluorescent turn-on chemosensors for detection of $Al^{3+}$ and $N_3^-$: Synthesis, photophysical and computational studies, *Luminescence*, 2018, **33**, 1194–1201, DOI: 10.1002/bio.3535.

23 A. D. Becke, Density-functional thermochemistry. III. The role of exact exchange, *J. Chem. Phys.*, 1993, **98**, 5648–5652, DOI: 10.1063/1.464913.

24 C. Lee, W. Yang and R. G. Parr, Development of the Colle-Salvetti correlation-energy formula into a functional of the electron density, *Phys. Rev. B: Condens. Matter Mater. Phys.*, 1988, **37**, 785–789, DOI: 10.1103/PhysRevB.37.785.

25 M. Silva, F. Kamberovic, S. T. Uota, I.-M. Kovan, C. S. B. Viegas, D. C. Simes, K. N. Gangadhar, J. Varela and L. Barreira, Microalgae as Potential Sources of Bioactive Compounds for Functional Foods and Pharmaceuticals, *Appl. Sci.*, 2022, **12**, 5877, DOI: 10.3390/app12125877.

26 M. Silva, F. Kamberovic, S. T. Uota, I.-M. Kovan, C. S. B. Viegas, D. C. Simes, K. N. Gangadhar, J. Varela and L. Barreira, Microalgae as Potential Sources of Bioactive Compounds for Functional Foods and Pharmaceuticals, *Appl. Sci.*, 2022, **12**, 5877, DOI: 10.3390/app12125877.

27 Y. M. Hijji, R. Rajan, A. M. Shraim, B. Attili, S. Uota and F. Abebe, Selective and Sensitive Dual Chromogenic Cyanide and Fluorescent Azide Probe, *Photochem*, 2025, **5**, 12, DOI: 10.3390/photochem5020012.

28 K. Chomaničová, Š. Husár, K. Maráková and M. Sýkorová, Development and Validation of UV Spectrophotometric Method for Determination of Trimetazidine Dihydrochloride in Modified Release Tablet Formulation, *Pharm. Chem. J.*, 2022, **56**, 570–575, DOI: 10.1007/s11094-022-02673-4.

29 H. A. Benesi and J. H. Hildebrand, A Spectrophotometric Investigation of the Interaction of Iodine with Aromatic

Open Access Article. Published on 25 June 2025. Downloaded on 3/11/2026 6:26:33 AM.
This article is licensed under a Creative Commons Attribution-NonCommercial 3.0 Unported Licence.

Hydrocarbons, *J. Am. Chem. Soc.*, 1949, **71**, 2703–2707, DOI: 10.1021/ja01176a030.

30 W. Chen, H. Liang, X. Wen, Z. Li, H. Xiong, Q. Tian, M. Yan, Y. Tan and G. Royal, Synchronous colorimetric determination of $CN^-$, $F^-$, and $H_2PO_4^-$ based on structural manipulation of hydrazone sensors, *Inorg. Chim. Acta*, 2022, **532**, 120760, DOI: 10.1016/j.ica.2021.120760.

31 J. H. Park, R. Manivannan, P. Jayasudha and Y.-A. Son, Selective detection of cyanide ion in 100% water by indolium based dual reactive binding site optical sensor, *J. Photochem. Photobiol., A*, 2020, **397**, 112571, DOI: 10.1016/j.jphotochem.2020.112571.

32 J. Palanisamy, R. Rajagopal and A. Alfarhan, Selective and Effective Sensing of Cyanide Ion with no Interference in Water by Phenothiazine-indolium Fused Optical Sensor, *J. Fluoresc.*, 2025, **35**, 2719–2728, DOI: 10.1007/s10895-024-03715-8.

33 Q. Shi, S.-T. Wu, L. Shen, T. Zhou, H. Xu, Z.-Y. Wang, X.-J. Yang, Y.-L. Huang and Q.-L. Zhang, A Turn-On Fluorescent Chemosensor for Cyanide Ion Detection in Real Water Samples, *Front. Chem.*, 2022, **10**, 923149, DOI: 10.3389/fchem.2022.923149.

34 S. D. Padghan, L.-C. Wang, W.-C. Lin, J.-W. Hu, W.-C. Liu and K.-Y. Chen, Rational Design of an ICT-Based Chemodosimeter with Aggregation-Induced Emission for Colorimetric and Ratiometric Fluorescent Detection of Cyanide in a Wide pH Range, *ACS Omega*, 2021, **6**, 5287–5296, DOI: 10.1021/acsomega.0c05409.

35 V. Sharma, B. Sahu, U. Kumar Das and G. Kumar Patra, A reversible fluorescent-colorimetric malononitrile based novel Schiff-base chemosensor for visual detection of bicarbonate ion in aqueous solution, *Inorg. Chim. Acta*, 2023, **552**, 121491, DOI: 10.1016/j.ica.2023.121491.

36 O. Aduroja, R. Shaw and F. Abebe, A bis(rhodamine 6G)-based fluorescent sensor for $Hg^{2+}$: microwave-assisted synthesis, photophysical properties, and computational studies, *Res. Chem. Intermed.*, 2022, **48**, 1847–1861, DOI: 10.1007/s11164-022-04704-x.

37 J. Schindelin, I. Arganda-Carreras, E. Frise, V. Kaynig, M. Longair, T. Pietzsch, S. Preibisch, C. Rueden, S. Saalfeld, B. Schmid, J.-Y. Tinevez, D. J. White, V. Hartenstein, K. Eliceiri, P. Tomancak and A. Cardona, Fiji: an open-source platform for biological-image analysis, *Nat. Methods*, 2012, **9**(7), 676–682, DOI: 10.1038/nmeth.2019.

38 M. H. Shihan, S. G. Novo, S. J. Le Marchand, Y. Wang and M. K. Duncan, A simple method for quantitating confocal fluorescent images, *Biochem. Biophys. Rep.*, 2021, **25**, 100916, DOI: 10.1016/j.bbrep.2021.100916 (accessed December 19, 2024).

 This journal is © The Royal Society of Chemistry and the Centre National de la Recherche Scientifique 2025